Available online at www.sciencedirect.com
SCIENCE DIRECT®
Earth and Planetary Science Letters 246 (2006) 161–176
EPSL
www.elsevier.com/locate/epsl

The influence of magma ascent path on the texture, mineralogy, and formation of hornblende reaction rims

Brandon L. Browne [a,*], James E. Gardner [b]

[a] Department of Geological Sciences, California State University, Fullerton, CA 92834, USA
[b] Department of Geological Sciences, University of Texas Austin, Austin, TX 78712, USA

Received 30 April 2005; received in revised form 25 April 2006; accepted 1 May 2006

Editor: S. King

Abstract

Although hornblende reaction rims are widely used as a tool for evaluating magma ascent during volcanic eruptions, very few studies constrain the manner in which they form. This study investigates the influence of magma ascent path on the formation of hornblende reaction rims. To do this, we conducted isothermal (840 °C) decompression experiments using dacite pumice samples erupted in December 1989 from Redoubt volcano, Alaska. Experiments were first held within the hornblende stability field determined through phase equilibria experiments for 3 to 5 days before being decompressed to different pressures ranging from 100 to 2 MPa for 1 to 30 days before being quenched. Decompression was performed in either multiple, equal steps (constant rate) or in one single step. Results from multi-step experiments show that reaction rims form preferentially at pressures from 10 to 40 MPa, and that this favorable pressure range narrows and decreases with increased decompression duration. Hornblendes in multi-step experiments are tightly enclosed by fine-grained reaction rims composed of plagioclase and orthopyroxene crystals with high aspect ratios ranging from 1 to 12. For single-step experiments, reaction rims also form preferentially within a narrow pressure range (60–70 MPa), where they consist of medium-grained plagioclase, titanomagnetite, and orthopyroxene crystals with aspect ratios ranging from 1 to 6 that broadly surround subrounded hornblendes. Hornblendes from single-step experiments dropped to lower pressures (<40 MPa), however, are typically euhedral and tightly enclosed by fine-grained reaction rims composed of plagioclase and orthopyroxene with aspect ratios ranging from 1 to 12. Little or no titanomagnetite is observed in these rims. Reaction rim growth was not observed at pressures below 10 MPa, regardless of decompression style or experiment duration, suggesting that hornblende in magma stored at very shallow depth (<200 m) will not develop reaction rims due to the limited hornblende dissolution combined with extremely high viscosity of the near-solidus interstitial melt. Finally, we describe what is expected from several different magma ascent paths with respect to the texture, mineralogy, and thickness of hornblende reaction rims, as well as changes in hornblende modal abundance. Observations from dome samples emplaced during the 1989–1990 eruption of Redoubt are consistent with the mixing of slowly rising and intermittently stalling batches of magma with lesser amounts of fresh, rapidly ascending magma. This interpretation is also consistent with seismic observations from the eruption.

Keywords: hornblende reaction rims; magma ascent; decompression textures; Redoubt volcano

* Corresponding author. Tel.: +1 714 278 3054; fax: +1 714 278 7266.
E-mail address: bbrowne@fullerton.edu (B.L. Browne).

0012-821X/$ - see front matter © 2006 Elsevier B.V. All rights reserved.
doi:10.1016/j.epsl.2006.05.006

1. Introduction

A critical problem in understanding how volcanic eruptions occur is determining the manner and rate in which magma ascends through the shallow crust during eruption. The style of magma ascent affects many important characteristics of volcanic eruptions, including eruptive style [1,2], magma supply and withdrawal [3,4], earthquake type and occurrence [5], magma mixing [6,7], and mineralogical reactions in the rising magma [8–12]. Unfortunately, there are few studies that constrain ascent rates, making it difficult to properly evaluate current models for magma ascent.

One particularly significant reaction that occurs in ascending magma is the breakdown of hydrous minerals, such as hornblende. Hornblende, which contains ~2 wt.% H_2O in its crystal structure [13], crystallizes at depth in magma storage chambers, but becomes unstable and reacts with the surrounding melt during ascent as the concentration of dissolved water in the melt decreases at lower pressures [14]. If magma ascends at a sufficiently slow rate, a reaction rim of anhydrous minerals, such as pyroxene, plagioclase, and Fe–Ti oxides may develop around a crystal where it is in contact with melt (Fig. 1) [15].

Rutherford and Hill [15] have examined the rates of hornblende breakdown in response to magma ascent in significant detail by performing experiments using a hornblende-bearing dacite erupted at Mount St. Helens in 1980, in which samples were isothermally (900 °C and 860 °C) decompressed at constant rates from ~210 MPa (or approximately 8 km depth) to near-surface conditions. They also investigated the rates of breakdown as a function of residence time at two shallow pressures equivalent to those proposed for shallow magma storage beneath Mount St. Helens. These experiments provided valuable information about the rate of hornblende reaction rim formation that occurs during magma ascent, especially that slower decompression rates result in hornblende phenocrysts with progressively thicker reaction rims. Rutherford and Hill [15] used their calibrated reaction rate to estimate magma ascent rates from the 1980–1986 eruptions of Mount St. Helens. Since then, countless studies have employed this calibration to infer information about magma ascent during other volcanic eruptions [16–19]. However, reaction rim formation involves a complex interplay of many factors, suggesting that it should be sensitive to changes in a variety of mineral and melt characteristics, including composition, viscosity, water content, temperature, and pressure [e.g. [20]]. For example, since both the concentration of dissolved water in melt and melt viscosity vary during ascent, the texture and growth rate of resulting reaction rims may also vary during ascent. Because dissolved water content of the melt varies with pressure, and viscosity

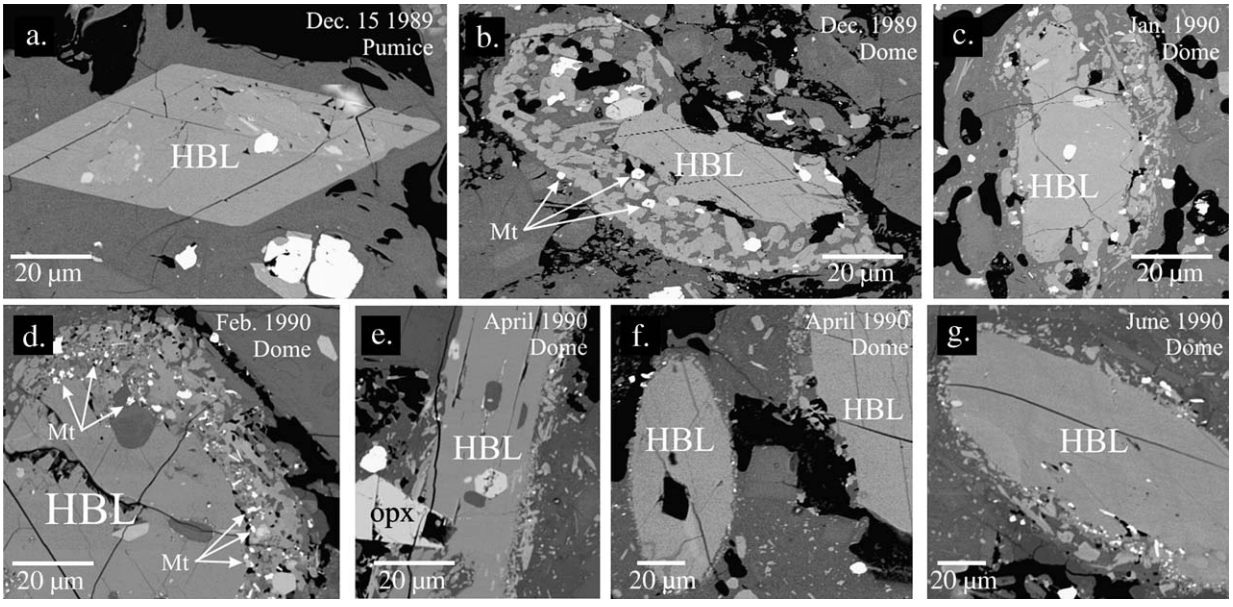

Fig. 1. BSE images of hornblende crystals from natural samples of 1989–1990 Redoubt eruption products with eruption dates provided. HBL, hornblende; opx, orthopyroxene; Pl, plagioclase; Mt, titanomagnetite. (a) Euhedral and unrimmed hornblende crystal from the December 15, 1989 plinian eruption phase (Sample 92MHR6-1); reaction rims surrounding hornblende crystals from domes emplaced on December 26, 1989 (b), January 2, 1990 (c), February 5, 1990 (d), April 15, 1990 (e, f), and June 20, 1990 (g). All reaction rims surround subrounded hornblendes.

varies strongly with water content of the melt, pressure is likely to be the main control of the reaction. Therefore, an understanding of reaction rim formation as a function of changing pressure during magma ascent is needed to quantitatively evaluate the effect of magma ascent path on reaction rim appearance and mineralogy.

To promote a more comprehensive understanding of hornblende reaction rim development during magma ascent, we conducted decompression experiments using dacite from the December 15, 1989 eruption of Redoubt volcano (Alaska). This starting material was selected for two main reasons. First, hornblendes in the 1989–1990 erupted material from Redoubt are surrounded by reaction rims of various thickness with distinctly different mineralogy and texture. These samples therefore provide an excellent opportunity to investigate the relationship between magma ascent path (decompression style) and the resulting texture and mineralogy of hornblende reaction rims. Second, although the bulk rock and matrix glass composition of Redoubt dacite are similar to many other recently erupted dome-forming magmas (Table 1) [21,22], including Mount St. Helens (1980, USA), Unzen volcano (1991, Japan), and Soufriere Hills (1995, Montserrat), the pre-erupted temperature of dacite magma erupted from Redoubt is appreciably cooler (~840 °C) than that erupted from Mount St. Helens in 1980 (~880 °C) and Unzen in 1991 (~860 °C). Thus, these samples also provide the chance to compare hornblende reaction rim formation at lower magma temperatures.

2. Experimental and analytical methods

Large portions of lightly crushed dacite pumice (92MHR6-1) erupted from Redoubt volcano on December 15, 1989 were selected as experimental starting materials. Like the majority of material produced from other dome-forming eruptions, Redoubt dacite contains ~35 vol.% phenocrysts of plagioclase, hornblende, orthopyroxene, titanomagnetite, and ilmenite. No hornblende phenocrysts in the dacite starting material contain reaction rims; although hornblende reaction rims are commonly observed in the 14 domes erupted between December 26, 1989 and June 20, 1990 [18,23,24].

Phase equilibria experiments were conducted to determine the stability field of hornblende, where equilibrium was determined by running reversal experiments. Isothermal decompression experiments were conducted to investigate how hornblende reaction rims form as a function of magma ascent path. In both sets of experiments, aliquots of powdered dacite were sealed in 3 or 4 mm $Ag_{70}Pd_{30}$ or Ag tubing along with a sufficient amount of distilled H_2O to make certain that all experiments were water saturated ($P_{total}=P_{H_2O}$) at the initial experimental pressure and temperature. All experiments were conducted in Ni-rich pressure vessels with a Ni filler rod and pressurized with H_2O to ensure an oxygen fugacity of approximately one log unit (±0.5) above the Ni–NiO (NNO) oxygen buffer curve [12]. Mineral phases were identified both optically and with energy

Table 1
Whole rock, glass compositions, and temperatures of recently erupted dome-forming magmas

Sample #	92MHR6-1	SH-118			92MHR6-1		91-4pumice	MON6ax
Volcano	Redoubt	Mount St. Helens	Unzen	Soufriere Hills	Redoubt	Mount St. Helens	Unzen	Soufriere Hills
Erupted event	12/15/1989	5/18/1980	Ave. comp. 5/91 to 5/95	Ave. comp. 12/95 to 10/97	12/15/1989	5/18/1980	May, 1991	January, 1996
	Pumice (WR) [37]	Pumice (WR) [21]	Pumice (WR) [22]	Pumice (WR) [16]	Pumice (G) [24]	Pumice (G) [38]	Pumice (G) [22]	Dome (G) [40]
SiO_2	63.44	63.81	65.24	60.02	76.58	72.49	74.42	71.41
Al_2O_3	17.67	17.46	15.94	17.86	12.72	14.60	11.25	13.58
TiO_2	0.46	0.62	0.65	0.60	0.24	0.36	0.37	0.28
FeO[a]	4.68	3.73	4.44	6.57	1.01	2.07	1.43	2.78
MnO	0.13	0.07	0.10	0.18	0..03	0.09	0.02	0.13
CaO	5.80	4.81	5.01	7.57	1.16	2.36	1.09	4.86
MgO	1.77	2.04	2.49	2.72	0.24	0.50	0.35	1.64
K_2O	1.68	1.26	2.42	0.82	3.44	2.18	3.97	1.60
Na_2O	4.18	4.99	3.54	3.50	3.93	5.16	2.77	3.73
P_2O_5	0.19	0.14	0.16	0.14	–	–	–	–
Total	100.00	98.93	99.99	99.98	99.35	99.81	95.67	100.01
Temp. (°C)	~840	~880 [39]	~860 [39]	~840 [16]				

[a] Total Fe is expressed as FeO; Wr: whole rock composition; G: matrix glass composition.

dispersive spectroscopy on the electron microprobe, and were considered stable based on the presence of new, euhedral crystals that grew during the experiment.

All isothermal decompression experiments were initially held for 3–5 days at pressure and temperature conditions ($P_{H_2O}=P_{total}$) within our determined hornblende stability pressure–temperature field, based on magnetite–ilmenite geothermometry (Table 2) and phase-equilibria experiments (Table 3) before carrying out the first pressure drop. Decompressions were performed in either single or multiple steps (Table 4), similar to the procedure employed by Hammer and Rutherford [11]. Single-step experiments were decompressed in one step to lower pressures ranging from 100 to 5 MPa and held for between 2 and 26 days before being quenched. Multi-step experiments were decompressed manually at rates of 30, 20, 10, 7, and 5 MPa/day using a controlled pressure intensifier in 2.5 to 10 MPa steps at 1 to 24 h intervals over 3 to 30 days to effect slow and quasi-constant decompression rates (~0.05–0.01 m/s) down to final pressures ranging from 70 to 2 MPa before being quenched. For these experiments, no extra time was spent at the final pressure.

After experimental runs, samples were mounted in epoxy on thin sections and polished. Back-scattered electron (BSE) images and mineral analyses were obtained from thin sections of natural and experimental samples using both a Cameca SX-50 electron microprobe (located at the University of Alaska, Fairbanks) and a JEOL 8200 (located at the University of Texas at Austin). BSE images were conducted using a 2-mm-wide focused beam, an accelerating voltage of 15 keV, and a beam current ranging from 25 to 50 nA. Titanomagnetite and ilmenite analyses were made using a 2-mm-wide focused beam, an accelerating voltage of 15 keV, and a beam current of 20 nA.

The widths of amphibole breakdown rims were measured in polished thin sections of both natural and experimental samples using back-scattered electron (BSE) imagery and reflected light analysis because they more clearly illustrate the true reaction rim, as noted by [15]. For newly grown rims, both microlites attached to the hornblende as well as those very near the hornblende that appeared to be part of the growth rim were included. Although subjective, the density of microlites within reaction rims is quite high compared to the groundmass (e.g. Fig. 1), making it easy to distinguish between microlites in the reaction rim and those in the groundmass. Reaction rims were measured in ~20 μm spacing along hornblende edges, resulting in between 20 and 50 measurements per crystal. These rim width measurements were then averaged. Reaction rims less than 1 μm thick could not be detected. All hornblende observed in each experimental sample were included in this study with the exception of crystals with damaged or cut margins resulting from

Table 2
Representative electron microprobe analyses (oxides in weight percent) of touching Fe–Ti oxide cores and rims

Sample	TiO_2	Al_2O_3	FeO[a]	Fe_2O_3[a]	MnO	MgO	Cr_2O_3	Total	Usp	Ilm	T (°C)	log fO_2
92MHR6-1 MT01 core	4.50	1.76	32.4	59.5	0.90	1.56	0.00	100.6				
92MHR6-1 MT01 rim	4.61	1.71	32.0	58.9	0.94	1.71	0.01	99.9	12.7			
92MHR6-1 ILM01 rim	31.14	0.28	23.3	41.7	0.81	2.21	0.08	99.5		57.7	843	−11.0
92MHR6-1 ILM01 core	34.60	0.30	26.2	35.1	0.83	2.29	0.06	99.4				
92MHR6-1 MT02 core	4.15	2.28	31.7	59.2	0.57	1.92	0.01	99.8				
92MHR6-1 MT02 rim	4.24	2.21	31.7	59.2	0.58	1.99	0.00	99.9	11.8			
92MHR6-1 ILM02 rim	34.41	0.38	23.6	43.6	0.42	1.89	0.00	100.3		56.4	839	−11.0
92MHR6-1 ILM02 core	34.47	0.40	27.3	35.0	0.39	1.88	0.02	99.5				
92MHR6-1 MT03 core	4.19	1.82	32.0	59.5	0.82	1.55	0.01	99.9				
92MHR6-1 MT03 rim	4.75	1.70	32.4	58.6	0.79	1.62	0.00	99.9	13.2			
92MHR6-1 ILM03 rim	30.91	0.20	23.3	43.3	0.72	2.14	0.00	100.6		56.7	850	−10.9
92MHR6-1 ILM03 core	35.69	0.26	27.7	33.3	0.67	2.08	0.01	99.7				
92MHR6-1 MT04 core	4.13	1.75	32.0	59.5	0.84	1.47	0.00	99.7				
92MHR6-1 MT04 rim	4.67	1.84	32.7	58.6	0.91	1.38	0.00	100.01	13.2			
92MHR6-1 ILM05 rim	31.91	0.28	25.3	39.9	0.72	1.48	0.00	99.6		60.0	840	−11.1
92MHR6-1 ILM05 core	33.72	0.21	26.1	36.8	0.71	1.99	0.00	99.5				
92MHR6-1 MT05 core	4.95	1.86	32.8	57.8	0.85	1.43	0.00	99.7				
92MHR6-1 MT05 rim	4.81	1.79	32.7	58.3	0.69	1.54	0.10	99.9	13.6			
92MHR6-1 ILM05 rim	32.78	0.27	25.0	39.7	0.76	2.10	0.00	100.6		60.3	842	−11.1
92MHR6-1 ILM05 core	34.98	0.29	26.8	34.4	0.83	2.16	0.00	99.5				

[a] Iron recalculation based on the method of Stormer [26] and calculated temperatures and oxygen fugacities for mineral pairs based on the method of Anderson and Lindsley [27]. Usp, mole fraction ulvospinel; Ilm, mole fraction ilmenite.

Table 3
Redoubt dacite phase equilibria experiments

Experiment	SM [a]	P (MPa)	T (°C)	Duration (days)	Products [b]
G-235	D	50	900	4.0	Pl, Opx, Ox, gl
G-237	D	150	780	9.6	Pl, Hbl, Opx, Ox, gl
G-238	D	100	840	7.0	Pl, Hbl, Opx, Ox, gl
G-240	D	200	780	7.7	Pl, Hbl, Opx, Ox, gl
G-244A	D	200	850	5.0	Opx, Hbl, Ox, gl
G-247A	D	200	900	2.8	Pl, Opx, Ox, gl
G-257A	D	125	850	6.8	Pl, Hbl, Opx, Ox, gl
G-258A	G-257A	125	825	5.8	Pl, Hbl, Opx, Ox, gl
G-296C	D	250	850	5.8	Pl, Hbl, Opx, Ox, gl
G-297C	G-240	200	800	8.8	Pl, Hbl, Opx, Ox, gl
G-301C	G-244A	200	825	10.8	Pl, Hbl, Opx, Ox, gl
G-301C	G-240	200	825	10.8	Pl, Hbl, Opx, Ox, gl
RDT-3	G-301C	125	850	4.9	Pl, Hbl, Opx, Ox, gl
RDT-4	D	150	840	5.0	Pl, Hbl, Opx, Ox, gl
RDT-10	RDT-4	150	880	4.5	Pl, Hbl, Opx, Ox, gl
RDT-11	RDT-4	100	880	4.5	Pl, Opx, Ox, gl
RDT-14A	D	125	875	5.1	Pl, Opx, Ox, gl
RDT-14B	G-257A	125	875	4.8	Pl, Hbl, Opx, Ox, gl
RDT-15	D	100	900	5.1	Pl, Opx, Ox, gl
RDT-16B	D	150	900	5.1	Pl, Opx, Ox, gl
RDT-17B	D	30	775	5.1	Solidus
RDT-21	RDT-4	90	840	8.2	Pl, Opx, Ox, gl
RDT-31B	G-301C	200	900	1.4	Opx, Hbl, Ox, gl
RDT-33	D	200	875	3.4	Pl, Hbl, Opx, Ox, gl
RDT-51	RDT-4	80	840	2.1	Pl, Opx, Ox, gl
RDT-77	D	250	900	2.0	Ox, gl
RDT-78	D	80	825	5.8	Pl, Opx, Ox, gl
RDT-79	RDT-16B	80	825	5.8	Pl, Opx, Ox, gl
RDT-80A	D	100	800	6.2	Pl, Hbl, Opx, Ox, gl
RDT-80B	RDT-17	100	800	6.2	Pl, Hbl, Opx, Ox, gl

[a] SM, Starting materials; D, crushed 12/15/89 dacite pumice 92MHR6-1; Experiment number, products of previous experiments used as SM.
[b] Pl, plagioclase; Hbl, horneblende; Opx, orthopyroxene; Px, orthopyroxene; Ox, Fe–Ti oxide; gl, glass.

the thin section making processes. Repeated measurements of hornblende rims indicate that the uncertainty (1σ) of this method is 10% of the mean value.

Size and shape measurements of crystals comprising amphibole breakdown rims were performed on selected natural and experimental samples by tracing their perimeters and calculating maximum and minimum diameters from BSE images using Scion Image software. A minimum of 15 reacting amphiboles from each sample was included in rim crystal measurement analyses. For each amphibole included, a minimum of 60 reaction rim crystals was measured. Reaction rim crystal size measurements were then used to calculate the aspect ratio (max length/min length) of each measured crystal within a given reaction rim.

Modal analyses of individual mineral phases observed in natural and experimental samples, including plagioclase, hornblende, orthopyroxene, Fe–Ti oxides, and matrix glass were performed by point counting 500 points on BSE images of each thin section (Table 5). Repeated measurements of modal abundances indicate an uncertainty (1σ) of 2% of the mean value.

3. Results

3.1. Geothermometry of natural samples

Titanomagnetite is abundant in dacite sample 92MHR6-1, occurring as 0.02 to 0.5 mm, euhedral to subhedral phenocrysts, or as inclusions in plagioclase, hornblende, and pyroxene. Although ilmenite is relatively rare, touching pairs of titanomagnetite and ilmenite are easily found. Titanomagnetite generally contains 6–9 wt.% TiO_2 (16–19 mol% ulvospinel) and grains in this sample are compositionally homogeneous (Table 2). Some dacite samples contain titanomagnetite grains with ilmenite exsolution lamellae, possibly representing an overprinting effect induced by cooling. All geothermometry estimates are limited to analyses of touching titanomagnetite and ilmenite grains with euhedral or subhedral crystal faces, no exsolution textures, and pair compositions potentially in equilibrium based on the model of Bacon and Hirschmann [25]. Geothermometry estimates from this study also employ the iron recalculation procedure of Stormer [26] and the algorithm of Anderson and Lindsley [27]. Sixteen titanomagnetite–ilmenite pairs from dacite sample 92MHR6-1 yield temperatures between 839 °C and 850 °C (average = 842 °C ± 5) and oxygen fugacities ranging from $10^{-10.6}$ to $10^{-11.6}$ bars (Table 2). These estimates are similar to those obtained in previous studies [18,24].

3.2. Hornblende reaction rims from natural samples

Hornblende is the most abundant mafic mineral in all 1989–1990 Redoubt samples, making up 4.5–5 vol.% of pumice samples from the initial eruption on December 15, 1989 [18,24]. All hornblende in dacite pumice are euhedral and lack decompression-induced reaction rims (Fig. 1). Unrimmed hornblendes also occur in dome samples emplaced throughout the Redoubt eruption, accounting for approximately 10 vol.% of all dome samples [18,28]. More commonly, however, reaction rims surround hornblende. This observation is similar to those made from other dome-forming eruptions [e.g. [15,16]].

Hornblende reaction rims observed in dome samples emplaced during the Redoubt eruption are distinguished

Table 4
Redoubt dacite isothermal decomposition experiments

Experiment	MS or SS	Rate	P_f (MPa)	Time (days)	Result	Rim products
RDT-1	MS	20 MPa/day	30	3.5	E Hbl, no rim	
RDT-2	MS	10 MPa/day	30	6.0	SR HBl, rim=2	Pl, Px
RDT-5	MS	30 MPa/day	10	3.0	E Hbl, no rim	
RDT-6	MS	20 MPa/day	80	1.5	E Hbl, no rim	
RDT-7	MS	10 MPa/day	5	4.0	SA Hbl, rim=5	Pl, Px
RDT-8	MS	10 MPa/day	70	1.5	E Hbl, no rim	
RDT-9	MS	10 MPa/day	50	4.9	SR and SA Hbl, no rim	
RDT-10	MS	10 MPa/day	20	8.5	SR and SA Hbl, rim=4	Pl, Px
RDT-11	MS	10 MPa/day	10	9.5	SR and SA Hbl, rim=5	Pl, Px
RDT-12	MS	7 MPa/day	2	14.8	SR and SA Hbl, rim=8	Pl, Px
RDT-13	MS	5 MPa/day	5	19.5	SR and SA Hbl, rim=15	Pl, Px, Mt (trace)
RDT-14	MS	5 MPa/day	70	6.6	SA Hbl, no rim	
RDT-15	MS	5 MPa/day	50	10.1	SR and SA Hbl, no rim	
RDT-16	MS	5 MPa/day	20	16.6	SR and SA Hbl, rim=2	Pl, Px, Mt (trace)
RDT-17	MS	5 MPa/day	10	18.5	SR and SA Hbl, rim=16	Pl, Px, Mt (trace)
RDT-18	SS		110	10.0	SR Hbl, no rim	
RDT-19	SS		85	4.3	SR Hbl, rim=trace	
RDT-20	SS		85	8.1	SR Hbl, rim=5	Pl, Px, Mt
RDT-21	SS		90	8.2	SR Hbl, no rim	
RDT-22		5 MPa/day	40	12.1	SR Hbl, rim=trace	
RDT-23		5 MPa/day	85	3.3	SR Hbl, no rim	
RDT-27	SS		10	6.8	SR Hbl, rim=4	Pl, Px
RDT-35	SS		60	7.5	SR Hbl, rim=12	Pl, Px, Mt
RDT-41		7 MPa/day	16	12.5	SR and SA Hbl, rim=7	Pl, Px
RDT-42		7 MPa/day	37	9.5	SR and SA Hbl, rim=trace	Pl, Px
RDT-43		7 MPa/day	58	6.5	SA Hbl, no rim	Pl, Px
RDT-44		7 MPa/day	79	3.5	SA Hbl, no rim	
RDT-46	SS		110	0.5	E Hbl, no rim	
RDT-47	SS		90	3.0	SR Hbl, no rim	
RDT-48	SS		75	3.0	SR Hbl, rim=trace	Pl, Px, Mt
RDT-49	SS		60	2.1	SR Hbl, rim=trace	Pl, Px, Mt
RDT-50	SS		100	2.1	E Hbl, no rim	
RDT-51	SS		80	2.1	SR Hbl, no rim	
RDT-52	SS		50	1.9	SA Hbl, no rim	
RDT-53	SS		40	1.9	SA Hbl, no rim	
RDT-54	SS		45	2.8	SR Hbl, rim=trace	Pl, Px, Mt (trace)
RDT-55	SS		20	2.0	SA Hbl, no rim	
RDT-58	SS		65	2.8	SR Hbl, rim=17	Pl, Px, Mt
RDT-59	SS		70	2.8	SR Hbl, rim=7	Pl, Px, Mt
RDT-60		7 MPa/day	9	13.5	SR and SA Hbl, rim=8	
RDT-63	SS		40	14.1	SA Hbl, rim=8	
RDT-64		20 MPa/day	5	7.2	SA Hbl, no rim	
RDT-65	SS		20	3.8	SA Hbl, rim=2	Pl, Px
RDT-68	SS		20	6.0	SA Hbl, rim=8	Pl, Px
RDT-69	SS		10	6.0	SA Hbl, rim=trace	Pl, Px
RDT-70	SS		30	9.9	SA Hbl, rim=15	Pl, Px
RDT-73	SS		20	17.0	SA Hbl, rim=15	Pl, Px
RDT-74	SS		30	17.0	SA Hbl, rim=26	Pl, Px
RDT-76	SS		5	26.0	SA Hbl, no rim	
RDT-81	SS		55	7.5	SR Hbl, rim=10	Pl, Px, Mt (trace)
RDT-82	SS		65	3.5	SR Hbl, rim=21	Pl, Px, Mt

Notes: MS, Multi-step experiment; SS, single-step experiment; Rate, decompression rate for MS experiments; *P*, final pressure (in MPa) at which experiment is quenched; Time, total time (in days) out of hornblende stability field; HBL rim in microns; E, euhedral edge; SR, subhedral, rounded edge; SA, subhedral angular edge; Hbl, hornblende; Pl, plagioclase; Px, orpthopyroxene; Mt, titanomanetite.

Table 5
Modal analyses of starting material and experimental samples

Sample	Type[a]	Event	P (MPa)	Phenocryst[b]					Counts	Modal abundance[c]				
				Pl	Hbl	Px	Ox	gl		% PI	% Hbl	% Px	% Ox	% gl
Starting material:														
92MHR6-1	P	Dec. 15, 1989		88	23	28	15	346	500	17.60	4.60	5.60	3.00	69.20
RDT-4	E		150	83	26	21	15	355	500	16.60	5.20	4.20	3.00	71.00
G-257A	E		125	89	25	23	14	349	500	17.80	5.00	4.60	2.80	69.80
RDT-3	E		125	89	24	22	16	349	500	17.80	4.80	4.40	3.20	69.80
Experimets:														
RDT-47	SS		90	217	23	23	15	222	500	43.40	4.60	4.60	3.00	44.40
RDT-20	SS		85	354	11	22	12	100	500	70.86	2.20	4.49	2.50	19.96
RDT-48	SS		75	355	13	25	13	95	500	71.00	2.50	5.00	2.50	19.00
RDT-59	SS		70	355	13	25	10	95	500	71.00	2.50	5.00	2.50	19.00
RDT-58	SS		65	360	15	23	13	93	500	72.00	3.00	4.50	2.00	18.50
RDT-82	SS		65	348	15	23	13	103	500	69.50	3.00	4.50	2.50	20.50
RDT-35	SS		60	398	18	20	13	53	500	79.50	3.50	4.00	2.50	10.50
RDT-81	SS		55	395	18	20	13	55	500	79.00	3.50	4.00	2.50	11.00
RDT-52	SS		50	400	20	23	13	45	500	80.00	4.00	4.50	2.50	9.00
RDT-54	SS		45	403	18	20	15	45	500	80.50	3.50	4.00	3.00	9.00
RDT-63	SS		40	398	18	23	15	48	500	79.50	3.50	4.50	3.00	9.50
RDT-74	SS		30	425	23	20	13	20	500	85.00	4.50	4.00	2.50	4.00
RDT-70	SS		30	408	20	25	15	33	500	81.50	4.00	5.00	3.00	6.50
RDT-73	SS		20	428	23	23	15	13	500	85.50	4.50	4.50	3.00	2.50
RDT-65	SS		20	425	23	23	13	18	500	85.00	4.50	4.50	2.50	3.50
RDT-68	SS		20	420	20	23	15	23	500	74.00	4.00	4.50	3.00	4.50
RDT-76	SS		5	430	23	23	15	10	500	86.00	4.50	4.50	3.00	2.00
RDT-6	MS	20 MPa/day	80	303	23	20	13	142	500	60.60	4.50	4.00	2.50	28.40
RDT-1	MS	20 MPa/day	20	328	23	23	15	112	500	65.60	4.50	4.50	3.00	22.40
RDT-64	MS	20 MPa/day	5	342	23	28	15	92	500	68.47	4.50	5.61	3.00	18.42
RDT-8	MS	10 MPa/day	70	251	23	20	15	191	500	50.25	4.50	4.00	3.00	38.24
RDT-9	MS	10 MPa/day	50	287	20	23	13	158	500	57.40	4.00	4.50	2.50	31.60
RDT-10	MS	10 MPa/day	20	307	18	20	18	138	500	61.40	3.50	4.00	3.50	27.60
RDT-11	MS	10 MPa/day	10	319	18	20	13	131	500	63.80	3.50	4.00	2.50	26.20
RDT-7	MS	10 MPa/day	5	346	18	23	13	101	500	69.27	3.50	4.50	2.50	20.22
RDT-44	MS	7 MPa/day	79	254	21	20	14	191	500	50.80	4.20	4.00	2.80	38.20
RDT-43	MS	7 MPa/day	58	261	19	23	13	185	500	52.20	3.80	4.50	2.50	37.00
RDT-42	MS	7 MPa/day	37	291	18	20	15	156	500	58.26	3.50	4.00	3.00	31.23
RDT-41	MS	7 MPa/day	16	297	18	18	15	152	500	59.46	3.60	3.50	3.00	30.43
RDT-12	MS	7 MPa/day	2	336	17	18	18	112	500	67.20	3.40	3.50	3.50	22.40
RDT-23	MS	5 MPa/day	85	219	23	20	15	223	500	43.84	4.50	4.00	3.00	44.64
RDT-14	MS	5 MPa/day	70	231	20	20	13	216	500	46.25	4.00	4.00	2.50	43.24
RDT-15	MS	5 MPa/day	50	236	18	23	15	209	500	47.20	3.50	4.50	3.00	41.80
RDT-23	MS	5 MPa/day	20	247	18	23	13	200	500	49.45	3.50	4.50	2.50	40.04
RDT-17	MS	5 MPa/day	10	264	16	23	15	182	500	52.85	3.20	4.50	3.00	36.44
RDT-13	MS	5 MPa/day	5	291	16	23	15	155	500	58.26	3.20	4.50	3.00	31.03

[a] Type: P, pumice; E, phase equilibria experiment; SS, single-step experiment sample; MS, multi-step experiment sample.
[b] Phenocryst: Pl, plagioclase; Hbl, horneblende; Px, orthopyroxene; gl, glass.
[c] Modal abundance: modal abundances based on 500 count points per sample.

based on texture, mineralogy, and thickness. Hornblende reaction rims from the first dome emplaced during the eruption on December 26, 1989 dome are 13 to 38 μm thick (Fig. 1b) and consist of 1–18 μm diameter plagioclase, orthopyroxene, and titanomagnetite with aspect ratios ranging from 1 to 6 (Fig. 2a). In contrast, hornblende reaction rims from domes emplaced during the middle of the 1989–90 eruption, such as those on January 2, 1990 and February 15, 1990, are 10–25 μm thick (Fig. 1c and d), and contain plagioclase, orthopyroxene, and titanomagnetite. Interestingly, these reaction rims are texturally bimodal with respect to the size (maximum diameter) and shape (aspect ratio) of the crystals comprising them (Fig. 2b and c). Whereas one population of reaction rim crystals resembles those observed in the December 26, 1989 dome samples with

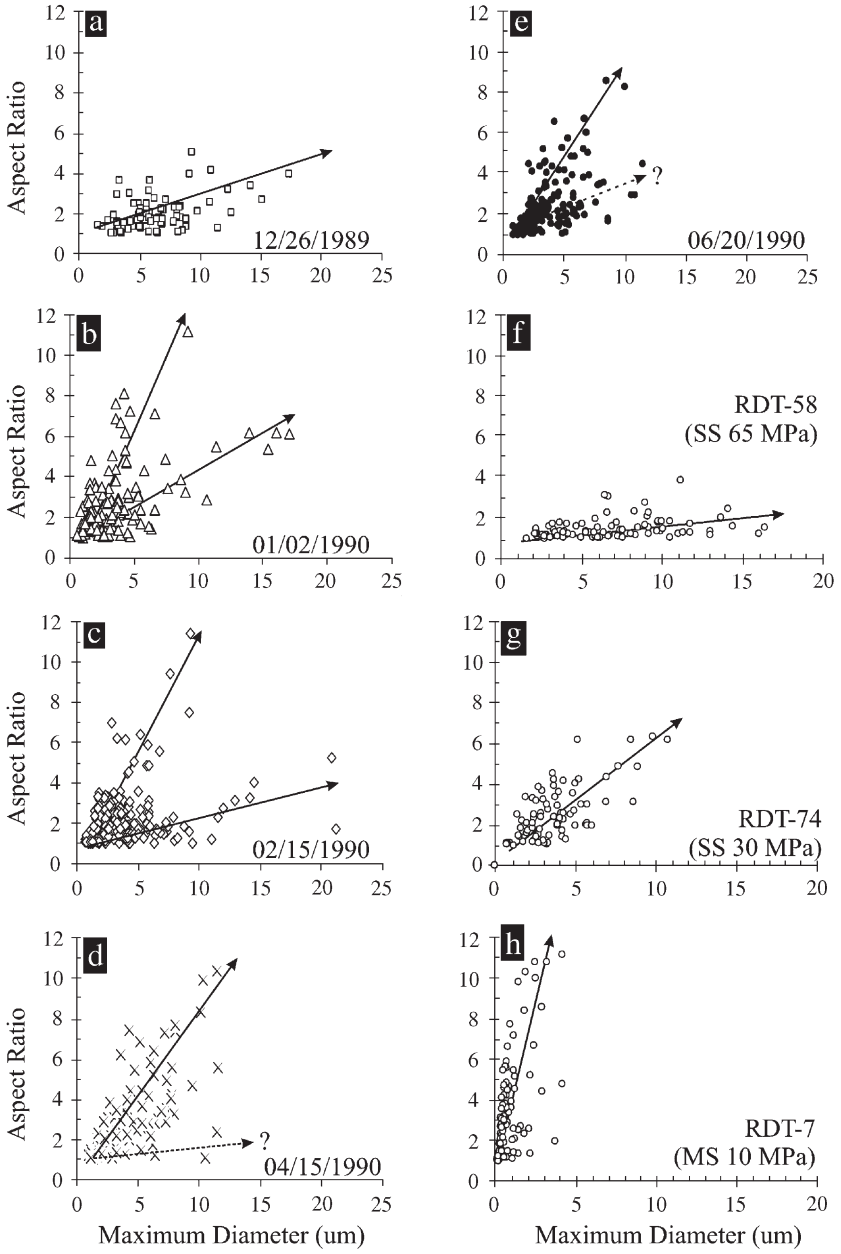

Fig. 2. Reaction rim crystal morphology plotted as a function of size (maximum diameter) and shape (aspect ratio) for reaction rims from natural and experimental samples. Plots include crystal morphology data from a minimum of 60 individual crystals contained in a representative hornblende reaction rim. Arrows indicate graphical trends in morphology. Reaction rim crystals from the December 26, 1989, dome are characterized by a single morphology trend (a), whereas those from the January 2, 1990 and February 15, 1990 are characterized by 2 distinct trends in morphology (b and c, respectively). Reaction rim crystals from the final domes emplaced on April 15, 1990 and June 15, 1990 appear to contain one dominant trend in rim morphology, although additional trends may exist as illustrated by dashed trend arrows (d and e, respectively). Reaction rim crystals become systematically more acicular and finer-grained with decreasing pressure as shown by the data from single-step (SS) and multi-step (MS) experiments decompressed to 65 MPa (f), 30 MPa (g), and 10 MPa (h).

relatively low aspect ratios (1–6) and diameters (1–22 μm), another population of crystals exists that is characterized by higher aspect ratios of 1–12 and smaller diameters ranging from 1 to 10 μm. Reaction rims from the final domes emplaced in the 1989–90 eruption, such as those on April 15, 1990 and June 20, 1990 range from 5 to 22 μm thick and are composed of plagioclase and orthopyroxene, with little or no

titanomagnetite (Fig. 1e–f, g). Most crystals observed in reaction rims from these samples are characterized by high aspect ratios (1–12) and smaller diameters (1–12 μm) (Fig. 2d and e). However, some crystals found in these reaction rims have anomalously low aspect ratios of 1–4 (Fig. 2d and 2 dashed arrows), resembling those found in earlier dome samples.

3.3. Experimental phase equilibria and hornblende stability

The results of the phase equilibria experiments on the Redoubt dacite are given in Table 3 and plotted in Fig. 3. Hornblende only crystallizes in the Redoubt dome dacite above 100 MPa at temperatures between 800 and 875 °C, and above 200 MPa at temperatures above 900 °C (Fig. 3). Plagioclase exists below 250 MPa at 860 °C and below 150 MPa at 900 °C, whereas low-Ca pyroxene is stable below 250 MPa at 880 °C. All dacite phase equilibria experiments contain titanomagnetite and ilmenite. Assuming a temperature of ~840 °C from magnetite–ilmenite geothermometry, we find that the natural assemblage is stable at pressures greater than 100 MPa, where hornblende breakdown begins below 100 MPa. Compositions of experimental plagioclase rims and matrix glass from dacite experiments run at 840 °C and 150 MPa (±25 MPa) are most consistent with plagioclase rims and matrix glass from the natural dacite pumice sample [28], further constraining storage of the natural dacite. Thus all decompression experiments were initially held at 840 °C and 150 MPa prior to the first pressure drop for 3 to 5 days. This pre-eruptive storage estimate correlates to a depth of 6–7 km, which is consistent with the depth approximation for magma storage of based on seismic evidence [29].

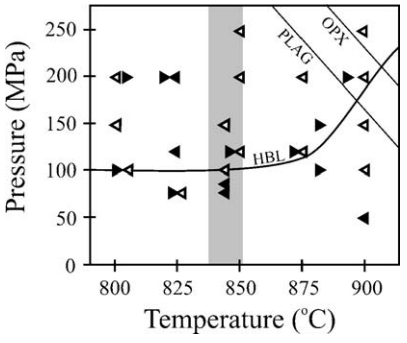

Fig. 3. Experimental phase equilibria diagram ($P_{H_2O}=P_{total}$) for hornblende in December 15, 1989 Redoubt dacite (92MHR6-1). Experiments are given by triangles, where open triangles are runs that used natural powder as starting material and solid triangles are reversal runs that used pre-annealed natural powder starting material from other runs; left- and right-pointing triangles represent crystallization and melting experiments, respectively. Solid lines are "mineral in" curves for hornblende plagioclase feldspar, and orthopyroxene. Fe–Ti oxides were observed in every run. The narrow, vertical darker shaded region brackets Fe–Ti oxide temperatures based on geothermometry.

3.4. Single-step decompression experiments

Single-step isothermal decompression runs produced a variety of breakdown rim mineralogy and textures depending on the final pressure of the experiment (Fig. 4, Table 4). Experiments held at 150 MPa and 840 °C for more than 3 days result in euhedral hornblende crystals with no reaction rims (Fig. 4a). Experiments decompressed to pressures between 80 and 90 MPa (20 to 10 MPa below hornblende stability) and held for 2 days are subrounded to rounded but do not contain reaction rims (Fig. 4b). Likewise, experiments decompressed to 70–60 MPa (30 to 40 MPa below the hornblende stability field) and held for 2 days contain unrimmed subrounded to rounded hornblende. However, those held for 3–5 days at these pressures contain subrounded hornblendes broadly surrounded by 5 to 18 μm thick reaction rims composed of titanomagnetite, orthopyroxene, and plagioclase (Fig. 4c and d) that range in diameter from 2 to 17 μm with aspect ratios of 1–4 (Fig. 2f). Experiments decompressed to 20 to 50 MPa (80 to 50 MPa below the hornblende stability field) and held for 2 to 10 days contain subangular hornblende with no reaction rims. Runs lasting 12 to 25 days, however, contain hornblende with breakdown rims 5 to 35 μm thick composed of orthopyroxene and plagioclase, with little or no titanomagnetite (Fig. 4e) ranging in diameter from 2 to 12 μm with aspect ratios of 1–7 (Fig. 2g). Reaction rims at this pressure tightly enclose the angular to subangular hornblende crystals, forming directly at the boundary between coexisting melt and crystal. Finally, experiments decompressed to 5 MPa (95 MPa below the hornblende stability field) consist of nearly euhedral hornblende with no reaction rims, even when held for as long as 26 days.

The rate of reaction rim growth into hornblende and the modal abundance of hornblende vary similarly in single-step decompression experiments. The growth rate of hornblende reaction rim aggregates ranges from 9×10^{-10} to 2×10^{-9} cm/s at 90–85 MPa and 5–55 MPa (Fig. 5a). Rim growth occurs at a faster rate, however, at pressures between 60 and 70 MPa, where it occurs at an average rate of 5×10^{-9} cm/s. In addition, hornblende modal abundance decreases from 4.6 vol.% to 2.2 vol.% in experiments decompressed to 90 and 85 MPa, respectively, which is notably less than that observed in phase equilibria experiments (4.6–5.2 vol.%) and

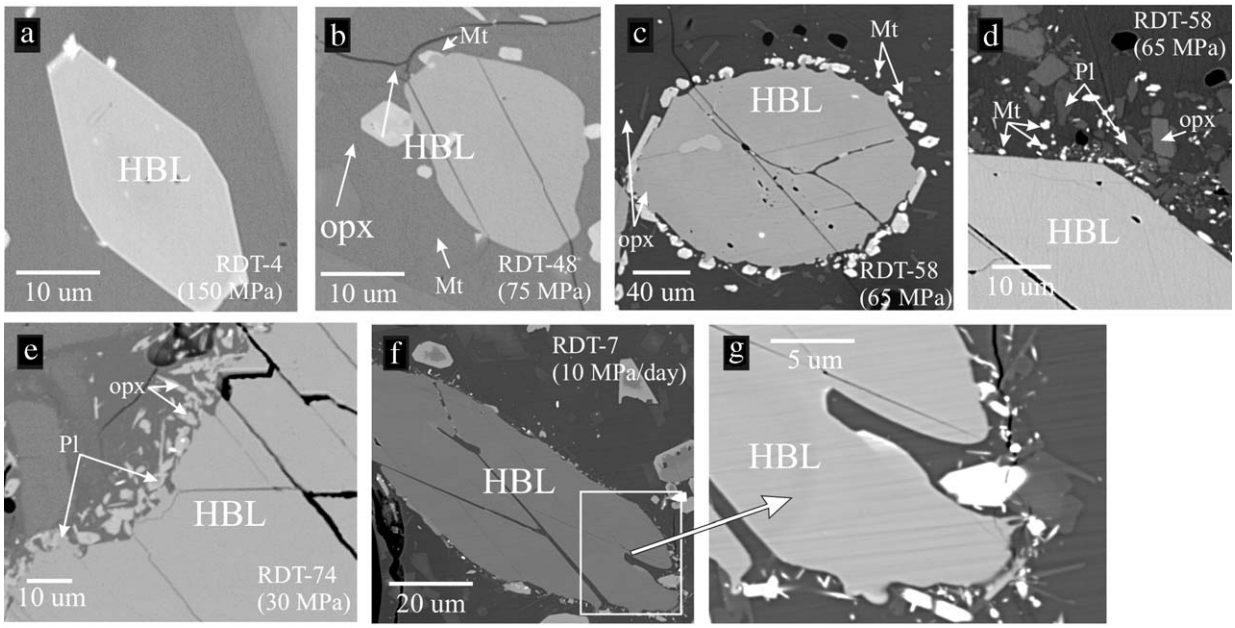

Fig. 4. BSE images of hornblende crystals from phase equilibria (a) and decompression (b–g) experiments, where experiment identification numbers are provided with the pressure that experiments were quenched. HBL, hornblende; opx, orthopyroxene; Pl, plagioclase; Mt, titanomagnetite. (a) Euhedral hornblende crystal from phase equilibria experiment RDT-4, (b) single-step experiment to 75 MPa, (c, d) single-step experiment to 65 MPa with high magnification view of plagioclase + orthopyroxene, and titanomagnetite reaction rim around subrounded crystal, (e) single-step to 30 MPa, and (f) multi-step experiment decompressed over 15 days at 10 MPa/day rate with high magnification view of plagioclase + orthopyroxene + titanomagnetite reaction rim around subrounded crystal (g). All reaction rims are fine-grained and composed of plagioclase and orthopyroxene, with variable amounts of titanomagnetite. Single-step experiments held at higher pressures (~60 MPa) for at least 3 days resulted in subrounded hornblendes with titanomagnetite-bearing reaction rims compared to single-step experiments quenched at lower pressures, which resulted in more angular hornblendes with reaction rims that typically lack titanomagnetite.

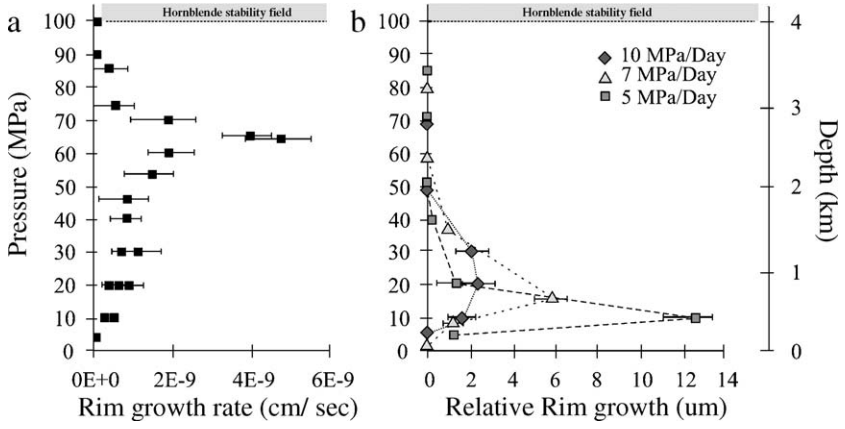

Fig. 5. Reaction rim growth plotted against pressure and corresponding depths (in km) for single-step (left) and multi-step (right) decompression experiments of the December 15, 1989 Redoubt dacite (Sample 92MHR6-1). Reaction rim growth rate is calculated by dividing the measured rim thickness by the total time held below the hornblende stability field (shaded), based on phase equilibria experiments. Relative rim growth is the difference in rim thickness from sequentially decompression experiments quenched at lower and lower pressures. For both decompression styles, growth rate is extremely slow near the hornblende stability field and at pressures below 10 MPa. Growth occurs at the fastest rate at pressures between 60 and 70 MPa, or 40 to 30 MPa below the hornblende stability field for single-step runs, whereas reaction rims form preferentially at lower pressures (10–50 MPa) for multi-step runs with increasing decompression duration.

December 15, 1989 dacite pumice starting material (4–5 vol.%) (Table 5). Likewise, experiments decompressed to 60–70 MPa also contain less modal hornblende (2.5 to 3.5 vol.%) compared to starting conditions. Finally, experiments decompressed to <50 MPa contain 3.5 to 5 vol.% hornblende, which is equivalent to the phase equilibria experiments and December 15, 1989 dacite pumice starting material.

3.5. Multi-step decompression experiments

Multi-step isothermal decompression experiments lasting 3 to 30 days produced reaction rim growth on hornblendes when decompressed to final pressures ≤30 MPa at rates ≤20 MPa/day, or at least 8 days out of the hornblende stability field (Fig. 4f and g, Table 4) in a transit from depth to the surface. Reaction rims form around subhedral crystal edges and are composed of orthopyroxene and plagioclase, with little or no titanomagnetite. These rims are uniformly fine-grained (0.2–5 μm) with a wide range in aspect ratio from 1 to 12 (Fig. 2h). Interestingly, reaction rims in these experiments formed preferentially at 30–10 MPa, where slower decompression rates result in rim growth at lower pressures (Fig. 5b). That is, during decompression rates of 10, 7, and 5 MPa/day, rims had average thicknesses of 5, 8, and 15 μm, respectively. Experiments decompressed at 20 or 30 MPa/day showed no change in modal hornblende compared to that observed in the starting material (4–5 vol.%) or phase equilibria experiments (4.6–5.2 vol.%). Hornblende modal abundance also slightly decreased in runs decompressed at 10, 7, and 5 MPa/day multi-step runs (Fig. 6).

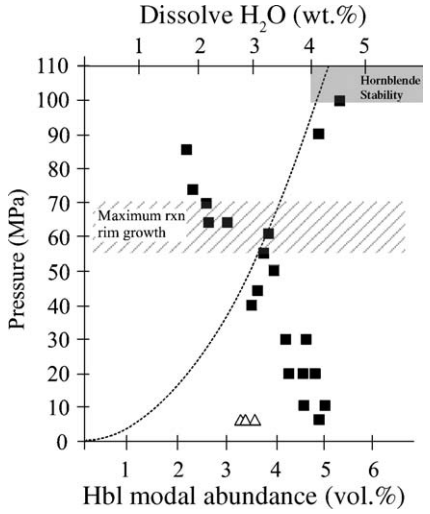

Fig. 6. Modal abundance of hornblende from single-step (filled squares) and multi-step (open triangles) decompression experiments as a function of pressure. Hatched pattern indicates region of maximum reaction rim growth and shaded region indicates region of hornblende stability field (HSF). Phase equilibria experiments performed within the HSF contain 4.2–5.5 vol.% hornblende phenocrysts (Table 4). Hornblende dissolution occurs strongly during single-step decompression at pressures between 60 and 85 MPa compared to pressures <40 MPa and >90 MPa or during multi-step decompression. At these conditions, hornblende dissolution is less significant. Crystallinity also varies with decompression style, increasing more rapidly with increasing decompression rate.

4. Discussion

4.1. Hornblende reaction rim formation

The mineral assemblage present in experimentally induced hornblende reaction rims that formed during decompression is identical to that of natural samples, as well as the existing phenocryst assemblage (Table 5). Reaction rims grow inward from the crystal edge with no breakdown in amphibole cores. These rims occur only when in contact with the surrounding melt, and not when amphibole is in contact with another crystal. This demonstrates that the formation of hornblende reaction rims is the result of a reaction between the hornblende crystal and the surrounding melt, most likely as a result of the reduction in the dissolved water content with decreasing pressure [15].

In the case of single-step decompression runs, the growth rate of hornblende reaction rims is highest 30 to 40 MPa below the hornblende stability field (60–70 MPa total pressure) and is characterized by steady growth of crystals to form the reaction rim as evidenced by their consistently low aspect ratio and wide ranging diameters (Fig. 2f). This pressure range also correlates to a region of elevated hornblende dissolution based on the presence of subhedral and rounded crystal edges and decreased modal abundance (Fig. 6). This implies that necessary reaction rim components released to the surrounding melt through hornblende dissolution enhance the formation rate of reaction rims.

The extent of hornblende dissolution, however, does not necessarily result in the formation of reaction rims, as evidenced by the lack of reaction rim formation at pressures where hornblende dissolution is greatest (75–90 MPa total pressure) for either single-step or multi-step runs. Hornblende dissolution clearly occurs at these conditions as indicated by subrounded to rounded crystal edges, and by the significant reduction in modal hornblende. This occurs simultaneously to increases in modal plagioclase, orthopyroxene, and titanomagnetite (Table 5), which possibly indicates that products of hornblende dissolution released to the

surrounding melt are transported away from the hornblende-melt boundary to crystal faces of other pre-existing minerals before crystallization of reaction rims can occur. This observation was also documented by Nicholis and Rutherford [30] in their work on hornblende breakdown in hawaiite magma, emphasizing transport effectiveness over breakdown rate in lower viscosity melts.

In contrast, hornblende dissolution is reduced at lower pressures, as indicated by the presence of subangular to angular hornblende crystals and the relatively high hornblende modal abundance. Declining dissolution with decreasing pressure is consistent with textures of the reaction rims. For example, in the case of multi-step decompression runs hornblende reaction rims grow fastest at 70 to 90 MPa below the hornblende stability field (30–10 MPa total pressure). At these conditions where dissolution is negligible, reaction rims are characterized by uniformly fine-grained (<5 μm) crystals with acicular habits, as noted by their high aspect ratios (1–12), that tightly enclose the subangular to angular hornblende crystal edges. The opposite is observed at higher pressures, where rims broadly surround (i.e. not necessarily in direct contact with) crystal edges in response to high degrees of dissolution. Below these pressures (0–10 MPa total pressure), reaction rims do not form at pressures in either single-step or multi-step runs, even when held for up to 26 days. This may seem contradictory to what is expected because these experiments occurred at conditions far below the amphibole stability limit. However, the interstitial melt at very low pressures (<10 MPa) contains very little dissolved water (<1 wt.%) and is almost entirely crystalline (Table 5), making it significantly more viscous (e.g. [13]). Hornblende reaction rims are thus unlikely to form at near-surface conditions (<10 MPa), regardless of the manner in which magma ascends, as a result of the lack of hornblende dissolution combined with the high melt viscosity and microlite-rich nature of the surrounding near-solidus interstitial melt.

4.2. Decompression path and hornblende reaction rims

A strong relationship exists between the decompression path and reaction rim formation rate (Fig. 5). This conclusion is consistent with observations from single-step runs where reaction rims form fastest at higher pressure, and from multi-step runs where reaction rims form fastest at lower pressures. It may seem illogical that given the same amount of time below the hornblende stability field, multi-step experiments, which were more slowly decompressed, resulted in favored growth of hornblende reaction rims at lower pressures compared to the rapidly decompressed single-step runs. However, this result is consistent with crystallization processes observed in other studies where thermodynamic driving forces (e.g. effective undercooling, disparate chemical potentials between hydrous crystals and dry melt) compete against kinetic barriers (namely melt viscosity) that restrict nucleation and crystal growth [8,11,31]. This is because for any given pressure drop during a decompression sequence, multi-step decompression produces smaller effective undercooling throughout the run than in the single-step experiments. Therefore, one should expect the thermodynamic driving forces in multi-step decompression experiments to be weaker, at least initially, compared to single-step runs.

A similar relationship exists between decompression path (ascent path) and the texture of the resulting reaction rim. This conclusion agrees with the influence that thermodynamic driving forces, such as effective undercooling, will have on the texture of crystallizing hornblende reaction rims. For example, with decreasing pressure, where the effective undercooling increases, reaction rim textures are finer grained and composed of progressively more acicular crystals (i.e. higher aspect ratios), relative to rims that form at higher pressures. This is evidenced by the distinct reaction rim textures produced during different decompression experiment scenarios (Fig. 2f–h). This observation is also consistent with other experimental studies where the dominant crystallization process changes during decompression to lower final pressures [11,32,33], emphasizing the effect that decompression path has on crystal texture.

4.3. Comparison to 1980–1986 Mount St. Helens dacite

Results from this study indicate that the growth of hornblende reaction rims in 1989–90 Redoubt dacite occurs 30–85% and 15–55% slower than experiments run at 900 °C and 860 °C, respectively, on Mount St. Helens 1980 dacite (Fig. 7). It is unlikely that this discrepancy results from hornblende composition, for hornblende phenocrysts from both magmas are generally equivalent with respect to composition and size [18]. Instead, results from this study indicate that reaction rim growth rate is strongly controlled by the rate at which rim components are supplied from the hornblende to the coexisting melt through dissolution of the crystal edges. Because this reaction was suppressed at low pressures, where interstitial melt was more viscous, it seems probable that the reaction rim growth

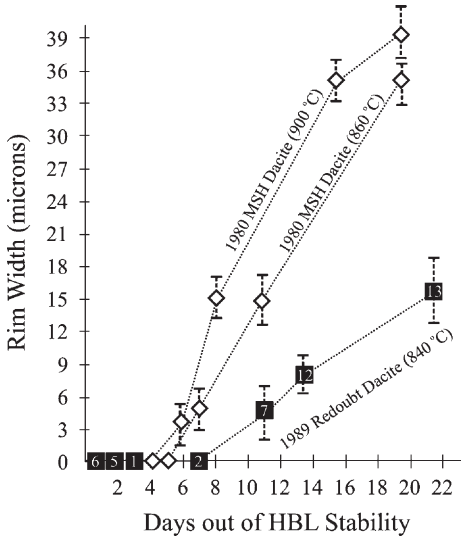

Fig. 7. Hornblende reaction rim width versus time below the hornblende stability field (HSF) for multi-step experiments on December 15, 1989 Redoubt dacite (Sample 92MHR6-1). Additional curves are for constant-rate decompression experiments at 900 °C and 860 °C on Mount St. Helens dacite performed by Rutherford and Hill [15]. The decompression-induced breakdown reaction of Redoubt hornblende is slower than those predicted for the Mount St. Helens dacite, indicating that Redoubt hornblende phenocrysts must spend more time outside the HSF in order to develop reaction rims of equivalent thickness to those observed at Mount St. Helens.

rate in hornblendes from 1989–90 Redoubt dacite was slower compared to those from 1980–86 Mount St. Helens dacite at equivalent pressures for similar reasons. This is consistent with the fact that decompression paths from Rutherford and Hill [15] are the same as those used in this study. Thus, changes in the dissolved water content of the melt during decompression are essentially the same also, indicating that differences in reaction rim formation in the 1989–1990 Redoubt dacite and the 1980–1986 Mount St. Helens dacite likely result from changes in melt viscosity arising from changes in temperature.

4.4. Implications for different magma ascent scenarios

A commonly used method for estimating magma ascent rate during a given eruption involves measuring the thickness of hornblende reaction rims and comparing them to the experimental calibration of rim width versus time for constant-rate decompression as outlined in Rutherford and Hill [15] (Fig. 7). Our results show, however, that hornblende reaction rims form at variable rates during ascent, or not at all at high (80–90 MPa) or very low (<10 MPa) pressures, suggesting that reaction rims of equivalent thickness may develop as a result of many different ascent scenarios, particularly if ascent rates are not constant.

We suggest that a more comprehensive interpretation of magma ascent path may be achieved through the combined examination of hornblende reaction rim texture, mineralogy, and thickness because each is expected to vary as a function of decompression rate, and whether magma was to stall at various depths (Fig. 8). For example, if magma rises directly from depth, reaction rim width is expected to increase as ascent rate slows (Ascent Paths 1 and 3, Fig. 8b). Reaction rim texture (grain size and aspect ratio) is also expected to vary as a function of ascent rate, where rims are likely to be finer-grained and more acicular as ascent rate slows (Ascent Paths 1 and 3, Fig. 8c). On the other hand, if rising magma periodically stalls at various depths during ascent, the width and texture of the resulting rim are expected to vary depending on the depth where stalling occurs. For example, stalling at depth results in coarser, more equant reaction rims, stalling at shallow depth results in fine-grained and acicular reaction rims, and stalling at near-surface conditions will result in no reaction rim growth (Ascent Paths 4, 5, and 2, respectively, Fig. 8). Finally, if magma were to stall repeatedly during ascent, hornblende reaction rims may develop textural and mineralogical zoning, with an outer zone that reflects rim formation at greater depth (e.g. equant and coarser-grained titanomagnetite-bearing rims) and an inner zone that reflects rim crystallization at shallower depth (e.g. acicular, finer-grained rims void of titanomagnetite).

4.5. Applications to the 1989–1990 redoubt eruptions

In order to apply these observations to interpretations of magma ascent during the 1989–1990 Redoubt eruptions, we have converted pressures to depths by assuming a density of 2600 kg/m^3. Hornblende reaction rims from the first dome emplaced at Redoubt on December 26, 1989 reflect an ascent path characterized by magma stalling at ~3 km depth during ascent (e.g. Fig. 8, Path 5) for approximately 3 days, based on the presence of reaction rims composed of large diameter crystals with uniformly low aspect ratios. This interpretation is consistent with textures observed in experiments held at 55–70 MPa during decompression (Fig. 2f), as well as seismicity during the December 26th eruption, which was localized at 3–6 km depth [29] in addition to the Redoubt summit. In contrast, hornblende reaction rims from domes emplaced during the January 2, 1990 and

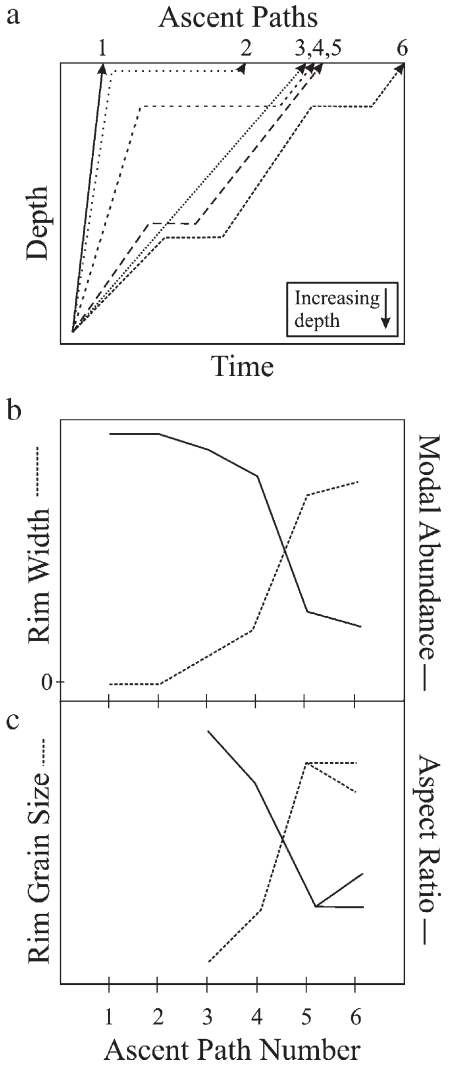

Fig. 8. Schematic diagram of 6 different magma ascent paths with time (a), where ascent paths and path numbers are indicated by arrows and corresponding numbers, respectively. Depth is plotted as increasing downwards. Path 1, magma ascending rapidly and directly to the surface at a constant rate; Path 2, magma ascending rapidly at a constant rate, stalling at very shallow depth for any given amount of time, then finally reaching the surface; Path 3, magma ascending slowly and directly to the surface at a constant rate; Path 4, magma ascending towards the surface, stalling at shallow depth for an extended period of time before continued ascent; Path 5, magma ascending towards the surface, stalling at intermediate depth briefly before continuing ascent; and Path 6, magma ascending towards the surface, stalling at intermediate depth, then again at shallow depth before reaching the surface. We indicate the expected reaction rim width and hornblende modal abundance (b), as well as reaction rim grain size and aspect ratio of reaction rim microlites (c) for each ascent path based on experimental results. See text for discussion.

February 15 1990 eruptions, reflect an ascent path characterized by magma stalling at ~3 km depth and then again at ~600 m during ascent (e.g. Fig. 8, Path 6) over a period of up to 15 days, based on the presence of 10–25 μm reaction rims composed of 2 populations of crystals characterized by either large diameter crystals with uniformly low aspect ratios or smaller crystals with higher aspect ratios. This is consistent with textures observed in experiments held at 55–70 MPa and 20–30 MPa (Fig. 2f and g) during decompression. Indeed, seismicity during these eruptions was observed in two discrete regions below the Redoubt summit, one at shallow depth (0–3 km) and another at deeper levels (3–6 km) [29]. Hornblende reaction rims from the final domes emplaced on April 15, 1990 and June 20, 1990 are 5–22 μm thick and composed of fine-grained and acicular plagioclase and orthopyroxene with only trace amounts of titanomagnetite. An ascent path that best describes these observations is one characterized by magma stalling at ~600 m depth for a period of up to 25 days (e.g. Fig. 8, Path 4). This is consistent with textures observed in experiments held at 20–30 MPa (Fig. 2g) during decompression as well as seismicity during these later eruptions, which was only observed at very shallow depth (0–3 km) [29].

Unrimmed hornblendes account for approximately 10 vol.% of all Redoubt dome samples [18,28]. In order to account for the presence of unrimmed hornblende in these dome samples, fresh magma rising at a sufficiently fast rate must have mixed with stalled conduit magma during ascent to the surface [e.g. [15]]. As a result, hornblendes from conduit-stalled magma will be incorporated as fresh batches of magma moved to the surface. The presence of crystals with anomalously large diameters and low aspect ratios in reaction rims from domes emplaced late in the eruption (e.g. Fig. 2d and e) is consistent with this model, for fresh rising magma batches are likely to incorporate stalled magma from all depths. This process is probably quite common, as evidenced by similarly diverse rim populations observed in other volcanoes, including Mount St. Helens, Washington [15,34], Popocatepetl, Mexico [35], Soufriere Hills, Montserrat [16,36], Tongariro Volcanic Centre, New Zealand [37], Black Butte, California [19], and the Crater Flat volcanic zone, Nevada [30]).

Acknowledgements

This paper has been significantly improved by reviews by Malcolm Rutherford, Julia Hammer, an anonymous reviewer, and Scott King. The interpretations of the data, however, are those of the authors, and not necessarily shared or endorsed by all

reviewers. Michelle Harbin and Kenneth Wolf collected Redoubt dacite pumice samples, while Christopher Nye, Alaska Volcano Observatory, and Samuel Swanson, University of Georgia, kindly provided thin sections of Redoubt dome and pumice samples. We thank Jessica Larsen, Malcolm Rutherford, Molly McCanta, Cynthia Gardner, Tom Sisson, Michelle Coombs, John Eichelberger, Heather Wright, Pavel Izbekov, Jonathan Castro, Barry Voight, Lindsay Szramek, and Carrie Browne for their rousing discussions and thoughtful encouragement of this study. We also are appreciative of Mount St. Helens for waking up after nearly 20 years, as a great deal of interest in hornblende reaction rims stirred awake as a result. Finally, we acknowledge the National Science Foundation (EAR-0106658) and the California State University, Fullerton Faculty Development Center for their financial support of this research.

References

[1] H. Sigurdsson, W. Cornell, S. Carey, Influence of magma withdrawal on compositional gradients during the AD 79 Vesuvius eruption, Nature 345 (1990) 519–521.

[2] C. Martel, M. Pichavant, J.L. Bourdier, H. Traineau, F. Holtz, B. Scaillet, Magma storage conditions and control of eruption regime in silicic volcanoes; experimental evidence from Mt. Pelee, Earth Planet. Sci. Lett. 156 (1998) 89–99.

[3] R. Scandone, S.D. Malone, Magma supply, magma discharge and readjustment of the feeding system of Mount St. Helens during 1980, J. Volcanol. Geotherm. Res. 23 (1985) 239–262.

[4] S. Carey, H. Sigurdsson, Temporal variations in column height and magma discharge rate during the 79 A.D. eruption of Vesuvius, Geol. Soc. Amer. Bull. 99 (1987) 303–314.

[5] A.L. Martin-del Pozzo, G. Cifuentes, Timing magma ascent at Popocatepetl Volcano, Mexico, 2000–2001, J. Volcanol. Geotherm. Res. 125 (2003) 107–120.

[6] A. Freundt, S.R. Tait, The entrainment of high-viscosity magma into low-viscosity magma in eruption conduits, Bull. Volcanol. 48 (1986) 325–339.

[7] T. Koyaguchi, S. Blake, The dynamics of magma mixing in a rising magma batch, Bull. Volcanol. 52 (1989) 127–137.

[8] C. Martel, B.C. Schmidt, Decompression experiments as an insight into ascent rates of silicic magmas, Contrib. Mineral. Petrol. 144 (2003) 397–415.

[9] K. Cashman, J. Blundy, Degassing and crystallization of ascending andesite and dacite, Philos. Trans. R. Soc., Lond. 358 (2000) 1487–1513.

[10] J.D. Blundy, R.S.J. Sparks, Generation, ascent and crystallization of calc-alkaline silicic magmas, Geochim. Cosmochim. 66 (2002) 83.

[11] J.E. Hammer, M.J. Rutherford, An experimental study of the kinetics of decompression-induced crystallization in silicic melt, J. Geophys. Res. 107 (2002) 1–24.

[12] C. Geschwind, M.J. Rutherford, Cummingtonite and the evolution of the Mount St. Helens (Washington) magma system; an experimental study, Geology 20 (1992) 1011–1014.

[13] W.A. Deer, R.A. Howie, J. Zussman, An Introduction to the Rock-Forming Minerals, 2nd edition, Addison Wesley Longman Limited, England, 1992. 248–253 pp.

[14] H.R., Shaw, Diffusion of H_2O in granitic liquids; Part 1, Experimental data; Part 2, Mass transfer in magma chambers, Carnegie Institution of Washington Pub. 634 (1974) 139–170.

[15] M.J. Rutherford, P.M. Hill, Magma ascent rates from amphibole breakdown; an experimental study applied to the 1980–1986 Mount St. Helens eruptions, J. Geophys. Res. 98 (1993) 19667–19685.

[16] J.D. Devine, M.J. Rutherford, J.E. Gardner, Petrologic determination of ascent rates for the 1995–1997 Soufriere Hills Volcano andesitic magma, Geophys. Res. Lett. 25 (1997) 3673–3676.

[17] A.S. Daag, M.T. Dolan, E.P. Laguerta, G.P. Meeker, C.G. Newhall, J.S. Pallister, R.U. Solidum, Growth of post-climactic lava dome at Mount Pinatubo, July–October, 1992, in: C.G. Newhall, R.S. Punongbayan (Eds.), Fire and Mud: Eruptions and Lahars of Mount Pinatubo, Philippines, University of Washington Press, Seattle, 1996, 647–664 pp.

[18] K.J. Wolf, J.C. Eichelberger, Syn-eruptive mixing, degassing, and crystallization at Redoubt Volcano, eruption of December, 1989 to May 1990, J. Volcanol. Geotherm. Res. 75 (1997) 19–38.

[19] M.C. McCanta, M.J. Rutherford, Black Butte, CA dacite dome; pre-eruption conditions, magma ascent, and links to Shasta, Eos, Trans. Am. Geophys. Union 80 (1999) 1106.

[20] M.L. Coombs, J.E. Gardner, Reaction rim growth on olivine in silicic melts; implications for magma mixing, Am. Mineral. 89 (2004) 748–759.

[21] M.J. Rutherford, J.D. Devine, The May 18 1980 Eruption of Mount St. Helens; 3. Stability and chemistry of amphibole in the magma chamber, J. Geophys. Res. 93 (1988) 11949–11959.

[22] S. Nakada, Y. Motomura, Petrology of the 1991–1995 eruption at Unzen; effusion pulsation and groundmass crystallization, J. Volcanol. Geotherm. Res. 89 (1999) 173–196.

[23] T.P. Miller, Dome growth and destruction during the 1989–1990 eruption of Redoubt volcano, J. Volcanol. Geotherm. Res. 62 (1994) 197–212.

[24] S.E. Swanson, C.J. Nye, T.P. Miller, V.F. Avery, Geochemistry of the 1989–1990 eruption of Redoubt Volcano: Part II. Evidence from mineral and glass chemistry, J. Volcanol. Geotherm. Res. 62 (1994) 453–468.

[25] C.R. Bacon, M.M. Hirschmann, Mg/Mn partitioning as a test for equilibrium between coexisting Fe–Ti oxides, Am. Mineral. 73 (1988) 57–61.

[26] J.C. Stormer, The effects of recalculation on estimates of temperature and oxygen fugacity from analyses of multicomponent iron–titanium oxides, Am. Mineral. 68 (1983) 586–594.

[27] D.J. Anderson, D.H. Lindsley, Internally consistent solution models for Fe–Mg–Mn–Ti oxides: Fe–Ti oxides, Am. Mineral. 73 (1988) 714–726.

[28] B.L. Browne, Petrologic and experimental constraints on magma mixing and ascent: examples from Japan and Alaska (Ph.D. Thesis), University of Alaska Fairbanks, 2005, 61–84 pp.

[29] J.A. Power, J.C. Lahr, R.A. Page, B.A. Chouet, C.D. Stephens, D.H. Harlow, T.L. Murray, J.N. Davies, Seismic evolution of the 1989–1990 eruption sequence of Redoubt Volcano, Alaska, J. Volcanol. Geotherm. Res. 62 (1994) 69–94.

[30] M.G. Nicholis, M.J. Rutherford, Experimental constraints on magma ascent rate for the Crater Flat volcanic zone hawaiite, Geology 32 (2004) 489–492.

[31] A.G. Simakin, P. Armienti, T.P. Salova, Joint degassing and crystallization; experimental study with a gradual pressure release, Geochem. Int. 38 (2000) 523–534.
[32] E. Dowty, Crystal growth and nucleation theory and the numerical simulation of igneous crystallization, in: R.B. Hargraves (Ed.), Physics of Magmatic Processes, Princeton University Press, Princeton, 1980, 419–458 pp.
[33] G. Lofgren, Experimental studies on the dynamic crystallization of silicate melts, in: R.B. Hargraves (Ed.), Physics of Magmatic Processes, Princeton University Press, Princeton, 1980, 493–542 pp.
[34] K.V. Cashman, S.M. McConnell, Multiple levels of magma storage during the 1980 summer eruptions of Mount St. Helens, WA, Bull. Volcanol. 68 (2005) 57–75.
[35] P. Athanasopoulos, The origin and ascent history of the 1996 dacitic dome, Volcan Popocatepetl, Mexico (Masters Thesis), University of Manitoba, Winnipeg, MB, Canada, 1997, pp. 38–42.
[36] M.J. Rutherford, J.D. Devine, Magmatic conditions and magma ascent as indicated by hornblende phase equilibria and reactions in the 1995–2002 Soufriere Hills magma, J. Petrol. 44 (2003) 1433–1454.
[37] M. Nakagawa, I.A. Nairn, T. Kobayashi, The approximately 10 ka multiple vent pyroclastic eruption sequence at Tongariro Volcanic Centre, Taupo Volcanic Zone, New Zealand: Part 2. Petrological insights into magma storage and transport during regional extension, J. Volcanol. Geotherm. Res. 86 (1998) 45–65.
[38] C.J. Nye, S.E. Swanson, V.F. Avery, T.P. Miller, Geochemistry of the 1989–1990 eruption of Redoubt Volcano: Part I. Whole-rock major- and trace-element chemistry, J. Volcanol. Geotherm. Res. 62 (1994) 429–452.
[39] M.J. Rutherford, H. Sigurdsson, S. Carey, A. Davis, The May 18, 1980, eruption of Mount St. Helens: 1. Melt composition and experimental phase equilibria, J. Geophys. Res. 90 (1985) 2929–2947.
[40] D.Y. Venezky, M.J. Rutherford, Petrology and Fe–Ti oxide reequilibration of the 1991 Mount Unzen mixed magma, J. Volcanol. Geotherm. Res. 89 (1999) 213–230.